Cardiel-Alvarez, M. A., Rodriguez-Amenedo, J. L., Arnaltes, S. & Montilla-DJesus, M. E. (2017). Modeling and Control of LCC Rectifiers for Offshore Wind Farms Connected by HVDC Links. *IEEE Transactions on Energy Conversion*, 32(4), pp. 1284–1296.

DOI: 10.1109/tec.2017.2696261

Modeling and Control of LCC Rectifiers for Offshore Wind Farms Connected by HVDC Links

Miguel Ángel Cardiel-Álvarez, Jose Luis Rodriguez-Amenedo, *Member, IEEE,*
Santiago Arnaltes and Miguel E. Montilla-DJesus, *Member, IEEE*

***Abstract*—This paper presents a voltage and frequency control (VFC) and an average-value model (AVM) of a line-commutated converter for a rectifier station in an offshore wind farm (OWF) connected by an HVDC link. A capacitor bank is placed at the AC terminals of the rectifier station to perform VFC within the OWF. The proposed model uses the active and reactive power generated by the OWF as inputs, while the state variables are the voltage magnitude and phase angle at the capacitor bank bus. The proposed VFC is based on the orientation of the voltage vector at the capacitor bank bus towards a synchronous reference axis. It is then demonstrated that frequency control is achieved by regulating the reactive power balance at the capacitor bank bus, while voltage control is carried out by regulating the active power balance. Moreover, it is demonstrated that in a diode rectifier, although voltage cannot be controlled as in a thyristor rectifier, it is bounded within acceptable limits. In addition, small-signal study is performed to facilitate controller design and system stability analysis. VFC and the accuracy of the proposed AVM are validated by simulation, using both the proposed AVM and a detailed switching model.**

***Index Terms*—Line-commutated converter (LCC), diode rectifier, HVDC, average-value model (AVM), offshore wind farm (OWF), frequency control, voltage control.**

I. Introduction

HIGH amounts of offshore wind power are expected to be generated in the near future. Offshore wind farms (OWFs) could exceed 1000 MW per plant and they will be located far from the coast. Because of the long sea transmission, high-voltage direct current (HVDC) links are more suitable than high-voltage alternating current transmissions [1].

Nowadays, two HVDC technologies are employed: voltage-source converters (VSCs), which use self-commutated switches like IGBTs, and line-commutated converters (LCCs), which use thyristors. VSCs offer operational advantages while LCCs are a mature technology [2]. In general, it is agreed that LCCs are superior to VSCs in terms of reliability, cost and efficiency [1]. In fact, due to the aforementioned advantages and to the complexity of VSCs, LCCs are being considered for HVDC transmission in future OWFs [3], [4].

Nevertheless, LCC-HVDC has several drawbacks. First, voltage and frequency have to be controlled in order to guarantee converter commutation given that the isolated grid of the OWF cannot generate the required voltage and frequency. Therefore, LCC-HVDC technology cannot be employed in an OWF with conventional wind turbine control. Moreover, this technology requires larger harmonic filters, which demand larger offshore platforms for the rectifier stations [5].

The literature proposes several offshore grid voltage- and frequency-control solutions. Most of the proposed solutions are based on the approach presented in [6], where voltage control in an OWF based on a doubly-fed induction generator (DFIG) is performed at the DFIG terminals, while frequency is controlled by adjusting the active power balance via the rectifier station's firing angle. Frequency control is based on the load-frequency relationship, though that only implies that a frequency change will produce a load change and not the opposite. This is true in a synchronous generator, where load variation provokes a change in frequency and this frequency variation in turn produces a load variation until a stable operating point is reached. A similar approach is employed in [7] and [8], but it is still not demonstrated how frequency changes in the system. In [9] and [10], an OWF with full converter wind turbine and diode rectifier station is employed. Frequency and angle are obtained from measurement at the AC terminals of the rectifier station and voltage and frequency control is oriented towards the resulting axis. Meanwhile, frequency control is achieved via an indirect method based on estimation of the rectifier reactive current demand, which requires the voltage, active and reactive power values at each individual wind turbine.

In [11], use of a large static synchronous compensator (STATCOM) is proposed to support voltage and frequency within the OWF. While in [12], a STATCOM is employed to control the active power balance within the OWF, based on the STATCOM DC voltage. Nevertheless, this requires a high DC capacity in order to minimize DC voltage fluctuations, which can be very large due to the high power variations in an OWF. In [13] and [5], two hybrid systems are presented. The first consists of an LCC-HVDC and current source converter (CSC) at the offshore end which regulates the offshore grid voltage and frequency. In the second, this control is carried out by a VSC placed in a DC series connection with a 12-pulse diode rectifier. Its power rating matches one third of the HVDC link rating and it is also used as an active filter.

The voltage and frequency control (VFC) proposed in this paper is based on decoupled control of voltage and frequency at the capacitor bank bus. VFC uses a synchronous reference axis where the voltage vector is decomposed into polar coordinates to obtain angle and magnitude, leading to decoupled frequency and voltage control. It is also demonstrated that

This work has been accomplished under Grant ENE2013-47296-C2-1-R: Offshore wind power integration in the Spanish power system by multiterminal HVDC links.

The authors are with the Department of Electrical Engineering, University Carlos III of Madrid, Madrid 28911, Spain (e-mail: mcardiel@ing.uc3m.es; amenedo@ing.uc3m.es; arnalte@ing.uc3m.es; mmontill@ing.uc3m.es).

frequency control is achieved by using the reactive power balance at the capacitor bank bus and that voltage control is achieved by using the active power balance at the same bus.

The VFC is derived from the proposed average-value model (AVM) of the LCC rectifier station and the HVDC link. The use of AVMs to represent and analyze systems which have power-electronics components is quite extended. This is due to the fact that detailed switching models require larger computing time than AVMs and it is hard to get their small-signal characteristics because of their discontinuous nature [14]. Average-value modeling of LCC converters connected to the stator of a synchronous machine were studied in [15]. Dq subtransient reactances are considered in the model. The stator dynamics is studied in the model proposed in [16]. In [17], a new approach which does not take into account the DC link smoothing inductor is presented, so constant DC current cannot be assumed. The previous studies are analytical, while parametric approaches considering the different conduction modes are used in [18], [19] and [20]. In [21], the LCC inverter operation is also considered. In addition, the parametric AVM approach has recently been extended to reconstruct the AC waveforms including system harmonics [22].

A comparison among the existing AVMs representing a diode rectifier load is presented in [23], but none of the evaluated models includes the AC filter capacitor dynamics. This paper presents an enhanced AVM of the LCC rectifier. In [24], the proposed AVM has an important drawback because the commutation resistance is physically included in the model, producing active power consumption that affects the active power balance within the converter. Nevertheless, this equivalent resistance is used to represent the DC voltage drop due to the AC inductance, so there should not be any power consumption [25]. The dynamic phasors technique allows considering harmonics, as it is presented in [26], [27] and [28]. An equivalent DC inductance, which includes the AC system inductance seen from the DC side, is also used in [26].

The novelty of the model proposed in this paper consists of representation of the AC voltage vector at the capacitor bank bus in polar coordinates referred to a synchronous reference axis which rotates at constant frequency. This axis is generated internally and therefore is not subjected to any grid disturbances or measurement noise. The inputs are the active and reactive power generated by the OWF, which are the conventional operation variables of wind turbines. The state variables are the phase angle and magnitude of the aforementioned voltage vector, which are the variables to be controlled in the OWF. This model permits analysis of the dynamic response of the rectifier station and HVDC link, considering the complete topology of the offshore grid by using a step-by-step load flow solution [29]. In these studies, the slack bus is the capacitor bank bus and the resulting active and reactive powers are the inputs to the dynamic model. The dynamic model produces the voltage at the slack bus that is used in the next step to obtain the new active and reactive power inputs.

The stability of the controlled system is analyzed using a small-signal study previously used to design the controller parameters. The accuracy of the AVM is validated by comparing the small-signal frequency response and large-signal time response of the AVM and a detailed switching model (DM) implemented in PSIM. Moreover, simulation results validate as well the proposed VFC. The paper is organized as follows. The proposed AVM of the system described in Section II is developed in Section III. Section IV presents the proposed control strategy. Then, in Section V the controllers are designed and stability is analyzed. Section VI presents simulation results using the proposed AVM and VFC. In Section VII, the proposed AVM and VFC are validated against the DM. In Section VIII, the fault response of the DM controlled system is evaluated. Finally, some conclusions are addressed in Section IX.

II. System Description

The system under study is presented in Fig. 1. The OWF rectifier station consists of an LCC rectifier connected through a transformer to a capacitor bank (C) and the required harmonic filters placed on the low voltage side. The OWF outputs are the active and reactive power, being this characteristic independent of the wind turbine technology (DFIG, full converter, etc.). Therefore, the OWF is represented by the active and reactive powers (P_g and Q_g, respectively) injected in the rectifier station bus. The HVDC link consists of a DC cable, an onshore inverter and the aforementioned rectifier. The inverter technology can be LCC or VSC, but it has to be operated in constant DC voltage mode.

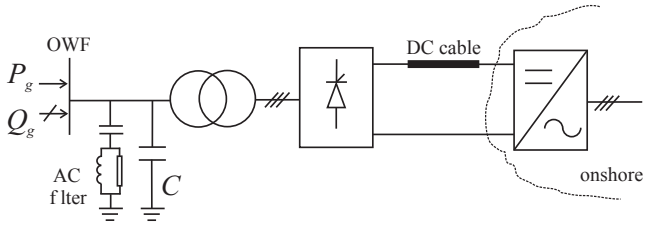

Fig. 1. LCC rectifier system under study.

III. LCC Rectifier Modeling

The following assumptions are considered in order to derive the AVM of the LCC rectifier station: Harmonics of AC and DC voltages and currents are neglected; the capacitor bank includes the reactive power compensation and the equivalent capacitance of the harmonic filters at the fundamental frequency [30]; there is no power loss in the AC-DC conversion; the LCC rectifier consists of a DC series connection of n_b 6-pulse bridges; the DC cable is modeled by the T-equivalent circuit given in the HVDC Benchmark Model [31]; and the onshore inverter of the HVDC link operates in constant DC voltage mode.

The aforementioned assumptions lead to the model proposed in Fig. 2, in which the three-phase current source i_{ga}, i_{gb}, i_{gc} represents the current injected by the OWF in the capacitor bank bus, the bus voltage being e_a, e_b, e_c. The current demanded by the rectifier station is i_{ra}, i_{rb}, i_{rc} and the AC transformer is depicted by its short-circuit inductance L_t. In the example in Fig. 2, one 6-pulse thyristor rectifier is

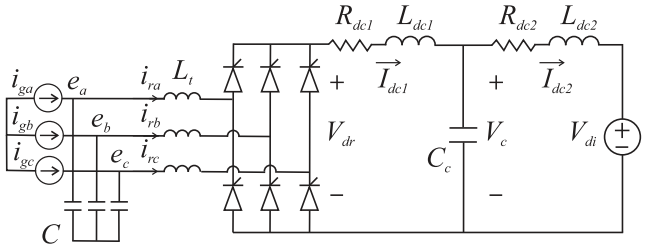

Fig. 2. LCC rectifier system to be modeled.

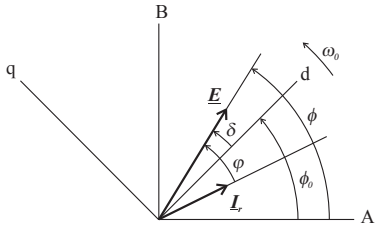

Fig. 3. Vector diagram in the stationary and synchronous reference systems.

represented (n_b equals 1) and the DC voltage at the rectifier output is V_{dr}. The DC cable is represented by its capacitance C_c and two resistive-inductive branches represented by R_{dc1}, L_{dc1}, R_{dc2} and L_{dc2}. V_{di} is the DC voltage input at the inverter station, and the DC cable model provides three additional variables: the rectifier DC current I_{dc1}, the DC capacitor voltage V_c and the inverter DC current I_{dc2}.

The AVM is derived in the following subsections for the general case of a thyristor rectifier, while the diode rectifier represents a particular case for a fixed firing angle equal to zero. These two technologies are considered in Section V to Section VIII. The model parameters have been taken from the HVDC Benchmark model [31] and they are detailed in Appendix A.

A. Synchronous Reference Model

The synchronous reference model is derived in this subsection. The Park transformation defined in (1) provides the transformation of AC currents and voltages into the dq reference frame.

$$\boldsymbol{T}(\theta(t))=\sqrt{\frac{2}{3}}\begin{bmatrix}\cos(\theta(t)) & -\sin(\theta(t))\\ \cos(\theta(t)-\frac{2\pi}{3}) & -\sin(\theta(t)-\frac{2\pi}{3})\\ \cos(\theta(t)+\frac{2\pi}{3}) & -\sin(\theta(t)+\frac{2\pi}{3})\end{bmatrix}^{\mathsf{T}} \quad (1)$$

where $\theta(t)=\omega_0 t-\frac{\pi}{2}+\phi_0$, ω_0 is the frequency of the synchronous axis and ϕ_0 is the angle between the synchronous and stationary systems, as shown in Fig. 3.

The state variables of the system are the voltage vector at the capacitor bank $\underline{\boldsymbol{E}}$, the voltage at the cable capacitance V_c and the DC currents at the rectifier output and the inverter input, I_{dc1} and I_{dc2}, respectively. The dynamic equation of the voltage vector at the capacitor bank bus is given in (2).

$$\underline{\boldsymbol{I_g}}-\underline{\boldsymbol{I_r}}=C\frac{d\underline{\boldsymbol{E}}}{dt}+\mathrm{j}\omega_0\mathrm{C}\underline{\boldsymbol{E}} \quad (2)$$

where $\underline{\boldsymbol{I_g}}$ and $\underline{\boldsymbol{I_r}}$ are the OWF and the LCC rectifier current vectors, respectively.

Equation (2) is split in its dq components in the set of equations representing the whole system dynamics presented in (3).

$$\begin{aligned}
I_{gd}-I_{rd}&=C\frac{dE_d}{dt}-\omega_0 CE_q\\
I_{gq}-I_{rq}&=C\frac{dE_q}{dt}+\omega_0 CE_d\\
V_{dr}-V_c&=R_{dc1}I_{dc1}+L_{dc1}\frac{dI_{dc1}}{dt}\\
I_{dc1}-I_{dc2}&=C_c\frac{dV_c}{dt}\\
V_c-V_{di}&=R_{dc2}I_{dc2}+L_{dc2}\frac{dI_{dc2}}{dt}
\end{aligned} \quad (3)$$

where d and q subscripts refer to the corresponding vector components.

AC and DC variables are related in the LCC rectifier. The relationships between AC and DC voltages and currents are given in (4) and they are derived from the Fourier analysis in [25] and [32]. The extra equations needed to obtain the variable $k_{\alpha,\mu}$ are detailed in Appendix B.

$$\begin{aligned}
V_{dr}&=\frac{3\sqrt{2}}{\pi}n_b k_{\alpha,\mu}E\cos\varphi\\
I_r&=\frac{\sqrt{6}}{\pi}n_b k_{\alpha,\mu}I_{dc1}
\end{aligned} \quad (4)$$

where E and I_r are the rms values of bus voltages e_a, e_b, e_c and rectifier currents i_{ra}, i_{rb}, i_{rc}, φ is the phase shift between the aforementioned voltages and currents, and α and μ are the firing and commutation angles, respectively.

Fourier analysis at the AC fundamental frequency (considering (4)) leads to the following relationships between AC and DC magnitudes in the LCC rectifier.

$$\begin{aligned}
V_{dr}&=\boldsymbol{S_{1,abc}}^{\mathsf{T}}\boldsymbol{E_{abc}}\\
\boldsymbol{I_{r,abc}}&=\boldsymbol{S_{1,abc}}I_{dc1}
\end{aligned} \quad (5)$$

where $\boldsymbol{E_{abc}}=[e_a(t)\quad e_b(t)\quad e_c(t)]^{\mathsf{T}}$, $\boldsymbol{I_{r,abc}}=[i_{ra}(t)\quad i_{rb}(t)\quad i_{rc}(t)]^{\mathsf{T}}$ and $S_{1,abc}$ is the switching vector as follows:

$$\begin{aligned}
\boldsymbol{S_{1,abc}}\quad=\quad&\frac{2\sqrt{3}}{\pi}k_{\alpha,\mu}n_b\\
&\cdot\big[\sin\gamma\quad\sin\big(\gamma-\frac{2\pi}{3}\big)\quad\sin\big(\gamma+\frac{2\pi}{3}\big)\big]^{\mathsf{T}}
\end{aligned} \quad (6)$$

where $\gamma=\omega_0 t+\phi-\varphi$, ϕ is the AC voltage phase angle.

Once the dq transformation in (1) is applied, (5) and (6) become:

$$\begin{aligned}
V_{dr}&=\boldsymbol{S_{1,dq}}^{\mathsf{T}}\boldsymbol{E_{dq}}\\
\boldsymbol{I_{r,dq}}&=\boldsymbol{S_{1,dq}}I_{dc1}
\end{aligned} \quad (7)$$

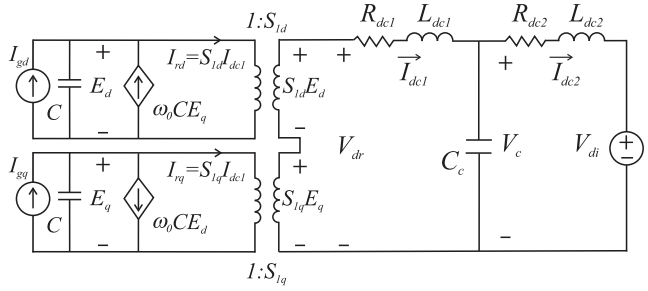

Fig. 4. Model of the system in a dq representation.

$$\boldsymbol{S_{1,dq}} = \frac{3\sqrt{2}}{\pi} n_b k_{\alpha,\mu} [\cos(\delta-\varphi) \quad \sin(\delta-\varphi)]^{\mathsf{T}} \tag{8}$$

where $\boldsymbol{S_{1,dq}}=\boldsymbol{T}(\theta(t))\boldsymbol{S_{1,abc}}=[S_{1d} \quad S_{1q}]^{\mathsf{T}}$ and δ is the angle between the AC bus voltage vector $\underline{\boldsymbol{E}}$ and the d axis ($\delta=\phi-\phi_0$), as it can be observed in Fig. 3.

Therefore, (7) is equal to the following expressions:

$$\begin{aligned} V_{dr} &= S_{1d}E_d + S_{1q}E_q \\ I_{rd} &= S_{1d}I_{dc1} \\ I_{rq} &= S_{1q}I_{dc1} \end{aligned} \tag{9}$$

These expressions, along with (3), yield to the dynamic equations given by (10). Fig. 4 shows the dq equivalent circuit.

$$\begin{aligned} I_{gd} - S_{1d}I_{dc1} &= C\frac{dE_d}{dt} - \omega_0 CE_q \\ I_{gq} - S_{1q}I_{dc1} &= C\frac{dE_q}{dt} + \omega_0 CE_d \\ S_{1d}E_d + S_{1q}E_q - V_c &= R_{dc1}I_{dc1} + L_{dc1}\frac{dI_{dc1}}{dt} \\ I_{dc1} - I_{dc2} &= C_c\frac{dV_c}{dt} \\ V_c - V_{di} &= R_{dc2}I_{dc2} + L_{dc2}\frac{dI_{dc2}}{dt} \end{aligned} \tag{10}$$

At this point, the dq model is transformed into a per-unit representation by using the base magnitudes and additional expressions presented in Appendix C. The resulting per-unit dynamic equations are detailed in (11)-(15). Note that lowercase notation is used to represent the per-unit magnitude of variables and parameters.

$$\frac{b_c}{\omega_0}\frac{de_d}{dt} = i_{gd} - k_{\alpha,\mu}i_{dc1}\cos(\delta-\varphi) + b_c e_q \tag{11}$$

$$\frac{b_c}{\omega_0}\frac{de_q}{dt} = i_{gq} - k_{\alpha,\mu}i_{dc1}\sin(\delta-\varphi) - b_c e_d \tag{12}$$

$$\begin{aligned} \frac{l_{dc1}}{\omega_0}\frac{di_{dc1}}{dt} &= k_{\alpha,\mu}(e_d\cos(\delta-\varphi) + e_q\sin(\delta-\varphi)) \\ &\quad - v_c - r_{dc1}i_{dc1} \end{aligned} \tag{13}$$

$$\frac{c_c}{\omega_0}\frac{dv_c}{dt} = i_{dc1} - i_{dc2} \tag{14}$$

$$\frac{l_{dc2}}{\omega_0}\frac{di_{dc2}}{dt} = v_c - v_{di} - r_{dc2}i_{dc2} \tag{15}$$

where $b_c=\omega_0 C Z_{base,ac}$ is the per-unit susceptance.

B. Polar Coordinates Model

This paper proposes modifying the above model by transforming its equations from Cartesian to polar coordinates, e_d and e_q being equal to $e\cos\delta$ and $e\sin\delta$, respectively. This transformation leads to a model whose state variables are the magnitude of capacitor-bank-bus voltage vector e and its phase angle δ, i.e. the variables to be controlled in order to maintain voltage and frequency in the offshore grid. Furthermore, the inputs of the model will be the active and reactive powers injected by the OWF in the aforementioned bus, as well as the firing angle of the thyristor rectifier and the DC voltage in the onshore inverter.

The relationships between the derivatives of the Cartesian and polar coordinates are as follows:

$$e\frac{de}{dt} = e_d\frac{de_d}{dt} + e_q\frac{de_q}{dt} \tag{16}$$

$$e^2\frac{d\delta}{dt} = -e_q\frac{de_d}{dt} + e_d\frac{de_q}{dt} \tag{17}$$

By introducing (11) and (12) in (16) and (17) and adjusting (13) to the new coordinate system, the final dynamic equations of the proposed model ((18)-(22)) are derived. Note that these equations will be used in Section V in the small-signal model and they have been named f_1 to f_5 for simplicity.

$$f_1 = \frac{1}{\omega_0}\frac{d\delta}{dt} = \frac{-q_g+q_r}{q_c} - 1 = \frac{-q_g}{b_c e^2} + \frac{k_{\alpha,\mu}i_{dc1}\sin\varphi}{b_c e} - 1 \tag{18}$$

$$f_2 = \frac{1}{\omega_0}\frac{de}{dt} = \frac{e}{q_c}(p_g - p_r) = \frac{p_g}{b_c e} - \frac{k_{\alpha,\mu}i_{dc1}\cos\varphi}{b_c} \tag{19}$$

$$f_3 = \frac{1}{\omega_0}\frac{di_{dc1}}{dt} = \frac{k_{\alpha,\mu}e\cos\varphi - v_c - r_{dc1}i_{dc1}}{l_{dc1}} \tag{20}$$

$$f_4 = \frac{1}{\omega_0}\frac{dv_c}{dt} = \frac{i_{dc1} - i_{dc2}}{c_c} \tag{21}$$

$$f_5 = \frac{1}{\omega_0}\frac{di_{dc2}}{dt} = \frac{v_c - v_{di} - r_{dc2}i_{dc2}}{l_{dc2}} \tag{22}$$

where $q_c=b_c e^2$ is the per unit reactive power of the capacitor bank, while $p_r=ei_r\cos\varphi=k_{\alpha,\mu}ei_{dc1}\cos\varphi$ and $q_r=ei_r\sin\varphi=k_{\alpha,\mu}ei_{dc1}\sin\varphi$ are the rectifier and transformer active and reactive power, respectively. In addition, $p_g=e_d i_{gd}+e_q i_{gq}$ and $q_g=e_q i_{gd}-e_d i_{gq}$ are the incoming OWF active and reactive power, respectively.

According to (18) and (19), the reactive and active power balances in the AC bus in which the capacitance is placed determine the dynamics of δ and e, respectively. These two expressions are used to derive the control strategy in Section IV. Furthermore, AC system frequency can be expressed as $\omega=\omega_0+\frac{d\delta}{dt}$. Then, (18) can be transformed into an explicit expression of frequency that depends on the reactive power balance in the capacitor bank bus:

$$\frac{\omega}{\omega_0}q_c = -q_g + q_r \tag{23}$$

Finally, Fig. 5 shows the input and output signals of the proposed AVM. This model includes the dynamic equations (18)-(22) and the algebraic equations (B.3), (C.10) and (C.11), detailed in Appendix B and Appendix C. Therefore, the input signals are the incoming OWF active and reactive power, the

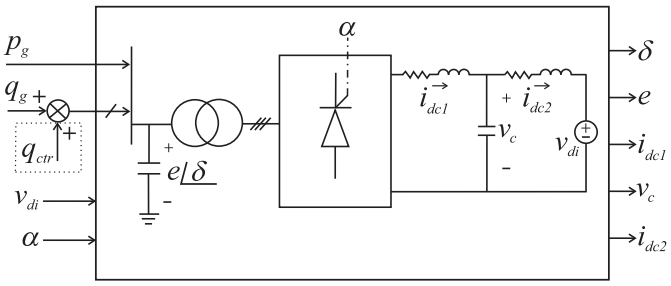

Fig. 5. Comprehensive input and output signals of the proposed AVM.

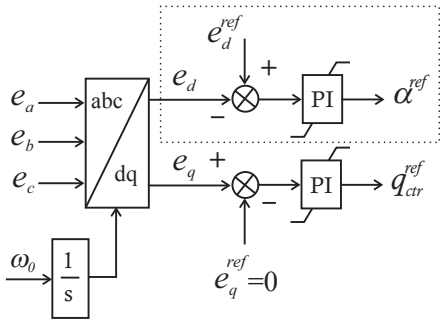

Fig. 6. Voltage and frequency control channels.

inverter DC voltage and the rectifier firing angle; while the outputs are the system states. Note that there is an extra input inside the dotted line (q_{ctr}) which will be introduced in the following section.

IV. Control Strategy

The objective of the control system is to maintain constant voltage and frequency within the OWF's AC grid. This paper proposes a decoupled control strategy whose principles are derived from the model dynamics in (18) and (19). Proportional-integral (PI) regulators are employed for both voltage and frequency control channels and the stability and performance of the controlled system are proven in the following sections.

A. Frequency Control

As stated in (18), the reactive power balance in the capacitor bank bus drives the dynamic response of the voltage vector phase angle δ in the synchronous reference frame. It should be pointed out that this synchronous axis is directly obtained by integrating desired fixed angular frequency ω_0, meaning that the reference angular position is not subject to measurement noise or grid disturbance because a phase-locked loop (PLL) is not needed. Therefore, frequency control is guaranteed by maintaining a constant angle δ for the voltage vector.

The reactive power balance in (18) contains two variables which cannot be controlled: q_c and q_r. The first is the reactive power generated by the capacitor bank, a passive element. The second is the reactive power drawn by the AC transformer and the rectifier, which mainly depends on the active power transmitted and the firing angle in the case of a thyristor rectifier. Reactive power q_g is one of the system inputs that depend on the OWF's active power and topology and the power factor settings at the wind turbine generators. However, additional reactive power q_{ctr} can be injected in the capacitor bank bus in order to align its voltage vector along the d axis (e_q=0 and δ=0) and achieve frequency control.

Reactive power q_{ctr}, whose reference value q_{ctr}^{ref} is set by the frequency control channel in Fig. 6, can be generated by any of the elements available in the OWF, e.g. the wind turbine generators or a device specifically employed for that purpose, such as a STATCOM. Adding q_{ctr} to the model derived in Section III provides the fifth input q_{ctr} shown inside the dotted line in Fig. 5 and modifies (18) and (23) as follows:

$$f_1 = \frac{1}{\omega_0}\frac{d\delta}{dt} = \frac{-q_g - q_{ctr}}{b_c e^2} + \frac{k_{\alpha,\mu} i_{dc1} \sin\varphi}{b_c e} - 1 \qquad (24)$$

$$\frac{\omega}{\omega_0} q_c = -q_g - q_{ctr} + q_r \qquad (25)$$

B. Voltage Control

According to (19), the voltage magnitude at the capacitor bank bus e depends on the active power balance in it. Considering that the active power generated by the OWF p_g is a function of wind speed and is not usually modified by control except in the case of power curtailment [33], the voltage control proposed is carried out by acting on the active power drawn by the LCC rectifier p_r by modifying firing angle α. Given that the onshore inverter operates in constant DC voltage mode, p_r increases when α decreases and vice versa.

As established in Section IV-A, the frequency control channel aligns the voltage vector with the synchronous axis and, in this situation, voltage magnitude e is equal to its d component e_d. Hence, voltage control sets the firing angle required to achieve reference voltage magnitude e_d^{ref}. This control channel is shown in Fig. 6 inside a dotted line because it cannot be applied in a diode rectifier. In this case, the voltage magnitude cannot be controlled. However, in steady-state it depends on the active power transmitted by the HVDC link and its variation is bounded between feasible values which are mainly influenced by onshore DC voltage v_{di} and DC link resistance. These effects can be observed in Section VI, where steady-state voltage is always within 0.95 p.u. and 1.05 p.u. which are voltage variations allowed in grid code worldwide [34].

Therefore, after introducing the proposed controls, from the inputs shown in Fig. 5, α and q_{ctr} are control inputs, while p_g, q_g and v_{di} are disturbance inputs.

V. Controller Design and Stability

Given that the dynamics of the LCC rectifier are non-linear, the PI parameters of the voltage and frequency controllers can be tuned using small-signal studies for each particular operating point. Since this methodology can become extremely cumbersome, the controller has been designed for one operating point and system stability is then checked in all other operating conditions. For the sake of simplicity, variable $k_{\alpha,\mu}$ in the proposed LCC rectifier model is kept constant with a value equal to steady-state for the small-signal studies [32].

The aforementioned process is performed in three stages. In the first, the plant is linearized without control, so the

state variables are $\boldsymbol{\Delta x}$=$[\Delta\delta, \Delta e, \Delta i_{dc1}, \Delta v_c, \Delta i_{dc2}]^\mathsf{T}$ and the inputs are $\boldsymbol{\Delta u}$=$[\Delta q_{ctr}, \Delta\alpha, \Delta p_g, \Delta q_g, \Delta v_{di}]^\mathsf{T}$. The first two are control inputs while the last three are independent inputs. In the second stage, frequency control is established for a diode rectifier case. Therefore, control input $\Delta\alpha$ does not exist and Δq_{ctr} becomes a function of $\Delta\delta$ through the frequency PI controller's dynamic equation. In the third stage, voltage and frequency control are considered for a thyristor rectifier case. Hence, control inputs Δq_{ctr} and $\Delta\alpha$ become functions of the states $\Delta\delta$ and Δe, respectively, given the dynamics of the proposed VFC. Note that although the diode rectifier can be considered as a particular case of a thyristor rectifier, the controlled systems are different because the thyristor rectifier includes an additional voltage controller.

A. Thyristor Rectifier and Diode Rectifier Systems

The LCC rectifier system's dynamic model is given by (19)-(22) and (24). For the small-signal study, these equations are linearized around a steady-state operating point in which the inputs are $\boldsymbol{u_0}$=$[q_{ctr0}, \alpha_0, p_{g0}, q_{g0}, v_{di0}]^\mathsf{T}$ and the states are $\boldsymbol{x_0}$=$[\delta_0, e_0, i_{dc10}, v_{c0}, i_{dc20}]^\mathsf{T}$. Note that subscript 0 denotes a steady-state value for the variable. After linearizing, the matrix form of the linearized system is as follows:

$$\begin{aligned} \frac{1}{\omega_0}\frac{d\boldsymbol{\Delta x}}{dt} &= \boldsymbol{A\Delta x} + \boldsymbol{B\Delta u} \\ \boldsymbol{\Delta y} &= \boldsymbol{C\Delta x} + \boldsymbol{D\Delta u} \end{aligned} \tag{26}$$

In order to linearize the system, the algebraic equation for angle φ (φ=$\arccos(\frac{1}{k_{\alpha,\mu}}(\cos\alpha - \frac{r_\mu i_{dc1}}{e})$) is needed to obtain $\boldsymbol{A}$ in (26), a 5x5 matrix whose non-zero elements are as follows:

$$\begin{aligned} a_{12} &= \frac{\partial f_1}{\partial e} = \frac{1}{e_0}\left(\frac{q_{r0}}{q_{c0}} - 2\right) + \frac{p_{g0}}{q_{c0}}\left(\frac{\partial\varphi}{\partial e}\right)_0 \\ a_{13} &= \frac{\partial f_1}{\partial i_{dc1}} = \frac{k_{\alpha,\mu}e_0\sin\varphi_0}{q_{c0}} + \frac{p_{g0}}{q_{c0}}\left(\frac{\partial\varphi}{\partial i_{dc1}}\right)_0 \\ a_{22} &= \frac{\partial f_2}{\partial e} = -\frac{p_{g0}}{q_{c0}} + e_0\frac{q_{r0}}{q_{c0}}\left(\frac{\partial\varphi}{\partial e}\right)_0 \\ a_{23} &= \frac{\partial f_2}{\partial i_{dc1}} = -\frac{k_{\alpha,\mu}e_0^2\cos\varphi_0}{q_{c0}} + e_0\frac{q_{r0}}{q_{c0}}\left(\frac{\partial\varphi}{\partial i_{dc1}}\right)_0 \\ a_{32} &= \frac{\partial f_3}{\partial e} = \frac{k_{\alpha,\mu}\cos\varphi_0}{l_{dc1}} - \frac{k_{\alpha,\mu}e_0\sin\varphi_0}{l_{dc1}}\left(\frac{\partial\varphi}{\partial e}\right)_0 \\ a_{33} &= \frac{\partial f_3}{\partial i_{dc1}} = -\frac{r_{dc1}}{l_{dc1}} - \frac{k_{\alpha,\mu}e_0\sin\varphi_0}{l_{dc1}}\left(\frac{\partial\varphi}{\partial i_{dc1}}\right)_0 \\ a_{34} &= \frac{\partial f_3}{\partial v_c} = -\frac{1}{l_{dc1}} \\ a_{43} &= \frac{\partial f_4}{\partial i_{dc1}} = -\frac{\partial f_4}{\partial i_{dc2}} = -a_{45} = \frac{1}{c_c} \\ a_{54} &= \frac{\partial f_5}{\partial v_c} = -\frac{1}{r_{dc2}}\frac{\partial f_5}{\partial i_{dc2}} = -\frac{a_{55}}{r_{dc2}} = \frac{1}{l_{dc2}} \end{aligned} \tag{27}$$

where $\left(\frac{\partial\varphi}{\partial e}\right)_0$=$\frac{1}{k_{\alpha,\mu}}\frac{-r_\mu i_{dc10}}{e_0^2\sin\varphi_0}$ and $\left(\frac{\partial\varphi}{\partial i_{dc1}}\right)_0$=$\frac{1}{k_{\alpha,\mu}}\frac{r_\mu}{e_0\sin\varphi_0}$.

The system outputs in (26) are $\boldsymbol{\Delta y}$=$[\Delta\delta, \Delta e, \Delta i_{dc1}, \Delta v_c, \Delta i_{dc2}, \Delta e_q]^\mathsf{T}$. $\boldsymbol{D}$ is a 6x5 zero matrix, while $\boldsymbol{C}$ is 6x5 matrix and consists of a 5x5 identity matrix with a sixth row equal to $[e_0\cos\delta_0, \sin\delta_0, 0, 0, 0]$. Finally, matrix $\boldsymbol{B}$ is a 5x5 matrix whose non-zero elements are as follows:

$$\begin{aligned} b_{11} &= \frac{\partial f_1}{\partial q_{ctr}} = b_{14} = \frac{\partial f_1}{\partial q_g} = -\frac{1}{q_{c0}} \\ b_{12} &= \frac{\partial f_1}{\partial\alpha} = \frac{p_{g0}}{q_{c0}}\left(\frac{\partial\varphi}{\partial\alpha}\right)_0 \\ b_{22} &= \frac{\partial f_2}{\partial\alpha} = e_0\frac{q_{r0}}{q_{c0}}\left(\frac{\partial\varphi}{\partial\alpha}\right)_0 \\ b_{23} &= \frac{\partial f_2}{\partial p_g} = \frac{e_0}{q_{c0}} \\ b_{32} &= \frac{\partial f_3}{\partial\alpha} = -\frac{k_{\alpha,\mu}e_0\sin\varphi_0}{l_{dc1}}\left(\frac{\partial\varphi}{\partial\alpha}\right)_0 \\ b_{55} &= \frac{\partial f_5}{\partial v_{di}} = -\frac{1}{l_{dc2}} \end{aligned} \tag{28}$$

where $\left(\frac{\partial\varphi}{\partial\alpha}\right)_0$=$\frac{1}{k_{\alpha,\mu}}\frac{\sin\alpha_0}{\sin\varphi_0}$.

The thyristor rectifier model given by (26) can be easily modified to represent a diode rectifier case by removing firing angle input $\Delta\alpha$. Therefore, the input vector becomes $\boldsymbol{\Delta u}$=$[\Delta q_{ctr}, \Delta p_g, \Delta q_g, \Delta v_{di}]^\mathsf{T}$ and the second column of matrices $\boldsymbol{B}$ and $\boldsymbol{D}$ is eliminated, while the rest of the elements in (26) remain the same.

B. Diode Rectifier System with Frequency Control

The frequency control proposed in Section IV consists of a PI controller which uses the q component voltage error to obtain a reactive power reference signal to be injected in the capacitor bank bus. Hence, the plant transfer function is the relationship between input Δq_{ctr} and output Δe_q in the small-signal system given at the end of Section V-A. This transfer function is a negative integrator with time constant τ=$\frac{b_c\cdot e_0^2}{\omega_0}$.

As stated before, the AC voltage in the diode rectifier case is not controlled. Consequently, the plant transfer function depends on the magnitude of the capacitor-bank-bus voltage vector for the operating conditions. In this paper, onshore inverter DC voltage v_{di} is adjusted to a value that yields the capacitor-bank-bus voltage to 1 p.u. when the DC link is transmitting approximately half its rated power. The parameters of the PI frequency controller are then designed at this operating point.

The controller time constant is set at 10 ms and the design specification is to obtain a feedback system with a bandwidth of 1000 rad/s.

The model with embedded frequency control can also be linearized to evaluate the stability of the system via its eigenvalues. The expression which depicts the PI frequency controller in the small-signal is presented in (30), where input Δe_q is defined in (29).

$$\Delta e_q = \Delta(e\sin\delta) = \Delta e\sin\delta_0 + e_0\cos\delta_0\Delta\delta = e_0\Delta\delta \tag{29}$$

$$\Delta q_{ctr} = e_0(k_p^f\Delta\delta + k_i^f\omega_0\int\Delta\delta dt) \tag{30}$$

where δ equals zero in steady-state and a new state has been defined: Δx_6=$\omega_0\int\Delta\delta dt$.

Frequency control adds a new dynamic equation ($f_6{=}\frac{1}{\omega_0}\frac{d\Delta x_6}{dt}{=}\Delta\delta$) to the system defined in (26), the new small-signal equations being as follows:

$$\frac{1}{\omega_0}\frac{d\boldsymbol{\Delta x'}}{dt} = \boldsymbol{A'\Delta x'} + \boldsymbol{B'\Delta u'}$$
$$\boldsymbol{\Delta y'} = \boldsymbol{C'\Delta x'} + \boldsymbol{D'\Delta u'} \tag{31}$$

where $\boldsymbol{\Delta x'}{=}[\Delta\delta, \Delta e, \Delta i_{dc1}, \Delta v_c, \Delta i_{dc2}, \Delta x_6]^\mathsf{T}$, $\boldsymbol{\Delta u'}{=}[\Delta p_g, \Delta q_g, \Delta v_{di}]^\mathsf{T}$ and $\boldsymbol{\Delta y'}{=}[\Delta\delta, \Delta e, \Delta i_{dc1}, \Delta v_c, \Delta i_{dc2}, \Delta q_{ctr}]^\mathsf{T}$.

The elements of 6x6 matrix $\boldsymbol{A'}$ are the same as in $\boldsymbol{A}$ plus the following changes:

$$a'_{i1} = a_{i1} + b_{i1}k_p^f e_0, \qquad (i = 1,2,3,4,5)$$
$$a'_{i6} = b_{i1}k_i^f e_0, \qquad (i = 1,2,3,4,5)$$
$$a'_{61} = 1$$
$$a'_{6i} = 0, \qquad (i = 2,3,4,5,6) \tag{32}$$

$\boldsymbol{B'}$ is a 6x3 matrix whose non-zero elements are derived from $\boldsymbol{B}$ as follows:

$$b'_{ij} = b_{i(j+2)}, \qquad (i = 1,2,3,4,5; \quad j = 1,2,3) \tag{33}$$

The aforementioned $\boldsymbol{\Delta y'}$ establishes that $\boldsymbol{D'}$ is a zero matrix with 6 rows and 3 columns, while $\boldsymbol{C'}$ is a 6x6 matrix whose non-zero elements are as follows:

$$c'_{ii} = 1, \qquad (i = 1,2,3,4,5)$$
$$c'_{61} = k_p^f e_0$$
$$c'_{66} = k_i^f e_0 \tag{34}$$

As the frequency controller has been designed for a specific operating point, the stability of the controlled system has to be proven for different steady-state conditions. In particular, a hundred operating points are studied between 0.01 p.u. and 1 p.u. of active power transmitted by the HVDC link. The system's eigenvalues for these cases are presented in Fig. 7. As the real part of the eigenvalues is negative, system stability in all operating conditions is proved. Furthermore, the arrows in Fig. 7 show how the system eigenvalues move as the active power increases and denote the dominant states. Note that the complex eigenvalues move towards more stable points when the transmitted power is increased because they are more damped. In addition, their dominant states are Δi_{dc1} and Δi_{dc2}, which are states with greater steady-state values in these varying conditions.

C. Thyristor Rectifier System with Voltage and Frequency Control

The thyristor rectifier system uses the frequency controller tuned in Section V-B as the plant is equal to that of the diode rectifier system. Given that voltage control permits a constant voltage to be maintained, this plant remains constant at all operating points.

The small-signal matrix representation of the system with frequency control is presented in (35). It is needed to derive the plant which has to be considered for voltage control design.

$$\frac{1}{\omega_0}\frac{d\boldsymbol{\Delta x''}}{dt} = \boldsymbol{A''\Delta x''} + \boldsymbol{B''\Delta u''}$$
$$\boldsymbol{\Delta y''} = \boldsymbol{C''\Delta x''} + \boldsymbol{D''\Delta u''} \tag{35}$$

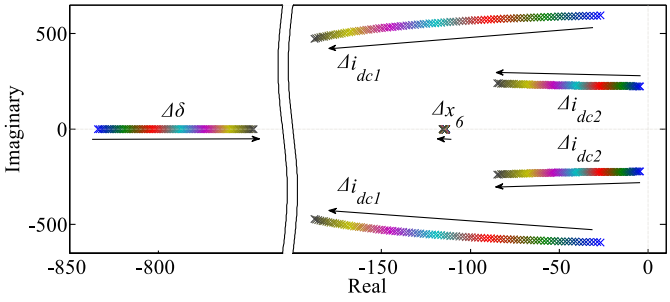

Fig. 7. Eigenvalues of the frequency-controlled diode rectifier system at different active-power operating points (arrows show increasing active power).

where $\boldsymbol{\Delta x''}{=}\boldsymbol{\Delta x'}$, $\boldsymbol{\Delta y''}{=}\boldsymbol{\Delta y'}$, $\boldsymbol{\Delta u''}{=}[\Delta\alpha, \Delta p_g, \Delta q_g, \Delta v_{di}]^\mathsf{T}$, $\boldsymbol{A''}{=}\boldsymbol{A'}$, $\boldsymbol{C''}{=}\boldsymbol{C'}$, $\boldsymbol{D''}$ is a 6x4 zero matrix and $\boldsymbol{B''}$ is equal to $\boldsymbol{B'}$ with the following column added on the left: $[b_{12}, b_{22}, b_{32}, b_{42}, b_{52}, 0]^\mathsf{T}$.

The PI voltage controller uses the negative d component voltage error Δe_d to obtain firing angle increment $\Delta\alpha$, as stated in Section IV. Note that the steady-state value of δ is zero and therefore Δe_d is equal to Δe ($\Delta e_d{=}\Delta e\cos\delta_0{-}e_0\sin\delta_0\Delta\delta{=}\Delta e$). The plant considered for this controller design is the open-loop transfer function in (35) between Δe and $\Delta\alpha$, which differs for each active-power operating point.

The controller is designed for a steady-state case where the rectifier is operating at half rated power. Firstly, the PI time constant is set at three times that of the frequency controller, i.e. 30 ms. Then, the controller proportional gain is tuned to yield a bandwidth in the feedback system of 500 rad/s.

The thyristor rectifier system with both control channels implemented can be linearized in order to determine its stability. For that purpose, the expression that defines the PI voltage controller is presented in (36).

$$\Delta\alpha = -(k_p^e\Delta e + k_i^e\omega_0\int\Delta e dt) \tag{36}$$

where a new state has been defined: $\Delta x_7{=}\omega_0\int\Delta e dt$.

The small-signal system for the thyristor rectifier case adds one extra dynamic equation ($f_7{=}\frac{1}{\omega_0}\frac{d\Delta x_7}{dt}{=}\Delta e$) to the ones used in (35) and is formulated as follows:

$$\frac{1}{\omega_0}\frac{d\boldsymbol{\Delta x'''}}{dt} = \boldsymbol{A'''\Delta x'''} + \boldsymbol{B'''\Delta u'''}$$
$$\boldsymbol{\Delta y'''} = \boldsymbol{C'''\Delta x'''} + \boldsymbol{D'''\Delta u'''} \tag{37}$$

where $\boldsymbol{\Delta x'''}{=}[\Delta\delta, \Delta e, \Delta i_{dc1}, \Delta v_c, \Delta i_{dc2}, \Delta x_6, \Delta x_7]^\mathsf{T}$, $\boldsymbol{\Delta u'''}{=}[\Delta p_g, \Delta q_g, \Delta v_{di}]^\mathsf{T}$ and $\boldsymbol{\Delta y'''}{=}[\Delta\delta, \Delta e, \Delta i_{dc1}, \Delta v_c, \Delta i_{dc2}, \Delta q_{ctr}, \Delta\alpha]^\mathsf{T}$.

The elements of 7x7 matrix $\boldsymbol{A'''}$ are the ones found in $\boldsymbol{A''}$ with the following changes:

$$a'''_{i2} = a''_{i2} - b''_{i1}k_p^e, \qquad (i = 1,2,3,4,5,6)$$
$$a'''_{i7} = -b''_{i1}k_i^e, \qquad (i = 1,2,3,4,5,6)$$
$$a'''_{72} = 1$$
$$a'''_{7i} = 0, \qquad (i = 1,3,4,5,6,7) \tag{38}$$

$\boldsymbol{B'''}$ is a 7x3 matrix whose non-zero elements are as follows: $b'''_{12}{=}b''_{13}$, $b'''_{21}{=}b''_{22}$ and $b'''_{53}{=}b''_{54}$. $\boldsymbol{D'''}$ consists of a matrix

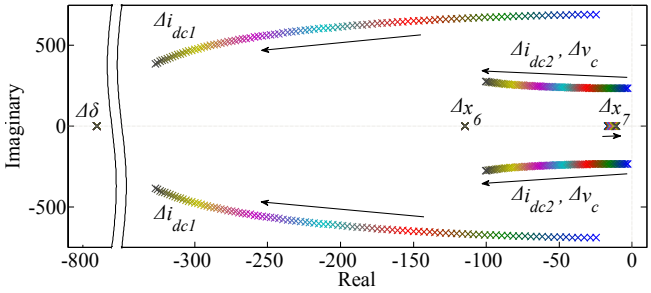

Fig. 8. Eigenvalues of the voltage- and frequency-controlled thyristor rectifier system at different active-power operating points (arrows show increasing active power).

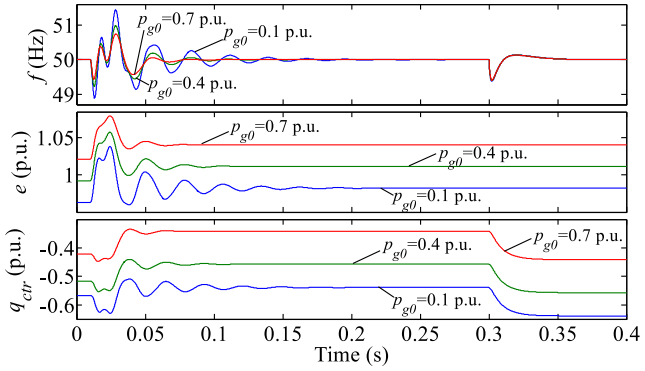

Fig. 9. Frequency, voltage and controlling reactive power during active- and reactive-power changes in the diode rectifier system.

with seven rows and three columns of zeros whereas $\boldsymbol{C'''}$ is equal to $\boldsymbol{C''}$ with an extra seventh row and column whose non-zero positions are as follows: $c'''_{72}{=}{-}k^e_p$ and $c'''_{77}{=}{-}k^e_i$.

The existing plant for the voltage controller design varies with rectifier active power. Therefore, the small-signal study is carried out for a hundred cases between values of 0.01 p.u. and 1 p.u. of power transmitted by the HVDC link. Analyzing the real part of the eigenvalues for these operating points, presented in Fig. 8, demonstrates that the plant is stable. The dominant states of each eigenvalue are also shown in Fig. 8. $\Delta\delta$ and Δx_6 are the dominant states of the two eigenvalues that are invariable with the operating conditions. Furthermore, the arrows in Fig. 8 denote the movement of the eigenvalues while the injected active power is increased. From the above, it is derived that system stability improves as power increases, because the complex eigenvalues are more damped. By comparing Fig. 7 and Fig. 8, it can be concluded that the two real eigenvalues affected by the operating conditions in the first case remain invariable for the thyristor rectifier case, due to the additional voltage controller. Moreover, Fig. 8 shows that the complex eigenvalues move even farther away from the imaginary axis than in the diode rectifier case. Also, Δv_c appears as a dominant state of one of the complex eigenvalues in Fig. 8.

VI. Average-Value Model Simulation Results

The proposed diode and thyristor rectifier and control models have been implemented in MATLAB/Simulink. This section evaluates those models' performance.

Both systems are simulated equally for 0.4 s. Three different initial operating conditions are considered with active powers equal to 0.1 p.u., 0.4 p.u. and 0.7 p.u. The reactive power initially injected by the OWF is zero in all cases. For the above conditions, two input steps are considered. The first consists of an active power increment of 0.2 p.u. at the capacitor bank bus at t=0.01 s (p_g). The second consists of a reactive power increment injected by the OWF (q_g) from zero to 0.1 p.u. at t=0.3 s. It should be pointed out that both input changes have been smoothed using a first-order filter with unitary gain and 10-ms time constant in order to represent a more realistic changing condition.

The simulation results obtained for both systems are presented and discussed in the following subsections.

A. Diode Rectifier System

The diode rectifier system simulation results are presented in Fig. 9 for the three study cases, each of them for the different initial load conditions. Fig. 9 shows frequency f, the magnitude of capacitor-bank-bus voltage vector e and the reactive power injected in the capacitor bank bus to control frequency q_{ctr}.

By analyzing the simulation results, it is concluded that voltage magnitude rises as a consequence of higher initial active power, provided that the onshore converter operates in constant DC voltage mode. The reactive power drawn by the rectifier also increases with the active power transmitted. Therefore, the reactive power to be injected for frequency control q_{ctr} also increases for each initial operating point.

At t=0.01 s, active power is increased and the values of e and q_{ctr} vary in the same direction, as expected with the aforementioned relationships. At t=0.3 s, the reactive power injected in the capacitor bank bus q_g changes from zero to 0.1 p.u. As can be seen in Fig. 9, voltage magnitude e is not affected by reactive power changes. Note that q_{ctr} decreases in order to balance the reactive power at the capacitor bank bus and to maintain constant frequency (reference value equal to 50 Hz).

It should be pointed out that the system's dynamic response to an increment in active power oscillates more when the initial conditions correspond to lower power transmission. This conclusion can be derived from Fig. 7, where the complex eigenvalues are damped when active power increases.

Moreover, Fig. 9 shows that although the voltage magnitude cannot be controlled, variance is bounded within acceptable limits. In fact, in steady-state the voltage limits reached are 0.954 p.u. and 1.05 p.u. when power transmission equals 0.01 p.u. and 1 p.u., respectively.

B. Thyristor Rectifier System

The simulation results for the thyristor rectifier system are presented in Fig. 10, where the variables of interest are frequency f, voltage magnitude at the capacitor bank bus e, reactive power injected in the bus to control the frequency q_{ctr}, and the firing angle α that controls the voltage magnitude. These variables are shown in Fig. 10 for the three initial operating points indicated at the beginning of this section.

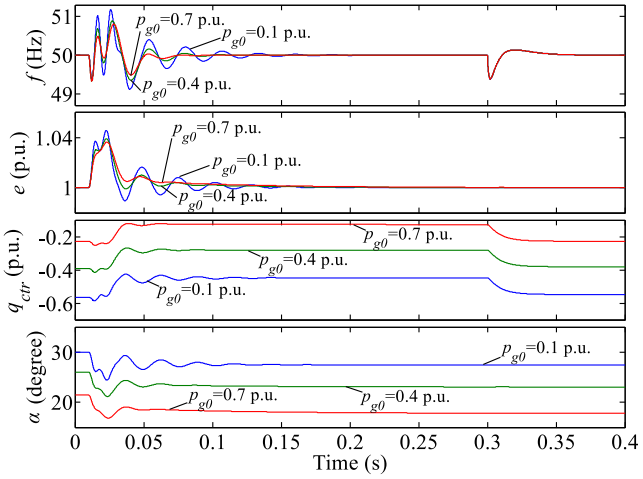

Fig. 10. Frequency, voltage, controlling reactive power and firing angle during active- and reactive-power changes in the thyristor rectifier system.

Fig. 10 shows that voltage and frequency are perfectly controlled at 1 p.u. and 50 Hz, respectively. On the other hand, the higher the active power transmitted by the HVDC link, the higher the reactive power required to control frequency q_{ctr} and the lower firing angle α required to control voltage. The same can be said after analyzing the response of q_{ctr} and α after the 0.2-p.u. increment in active power p_g at t=0.01 s.

Meanwhile, at t=0.3 s, OWF reactive power q_g is increased to 0.1 p.u. This mainly affects the frequency (affection of the voltage magnitude e is negligible). In any case, this response differs slightly from the diode rectifier system one, where voltage dynamics are completely decoupled from the change in reactive power.

Finally, it should be pointed out that the system's dynamic response oscillates more when active power is lower. This behavior can be observed in Fig. 10, which is consistent with the eigenvalues study derived in Section V-C.

In addition, it can be observed that q_{ctr} can reach high values in both simulation cases. This is due to the large passive AC capacity (harmonic filters and compensation capacitor bank) used in the HVDC Benchmark. As it was already stated, this q_{ctr} can be provided by the wind turbines, but additionally an STATCOM will also be needed because of the large amount of reactive power required. However, the AC capacitance could be reduced [35] in order to avoid the STATCOM.

VII. Control System and Model Validation

The detailed switching models (DMs) of the diode and thyristor rectifier systems under study have been implemented in PSIM in order to validate the performance of the proposed control system and determine the accuracy of the proposed AVM. In order to accomplish these validations, the small-signal frequency-domain and large-signal time-domain analysis of the AVM and DM controlled systems will be performed in the following subsections.

A. Small-Signal Frequency-Domain Analysis

The frequency response of the controlled diode and thyristor rectifier systems is analyzed in this subsection. This study is performed for both the AVM and the DM in order to compare their responses. For this purpose, the transfer function between the OWF active power and the rectifier DC current at a steady-state operating point of 0.4 p.u. of active power through the link is used.

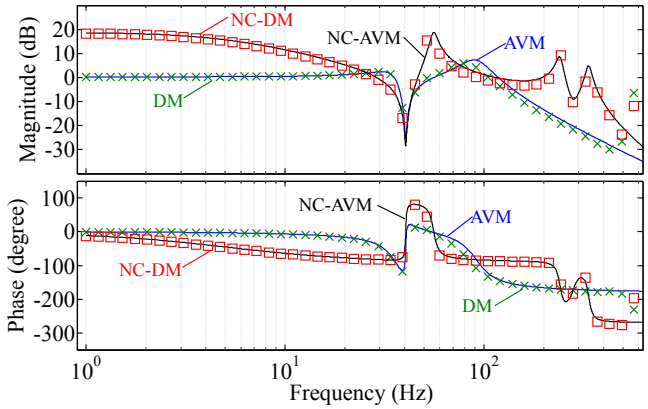

Fig. 11. Frequency response of the AVM and the DM controlled diode rectifier systems and non-controlled diode rectifier systems (NC-AVM and NC-DM).

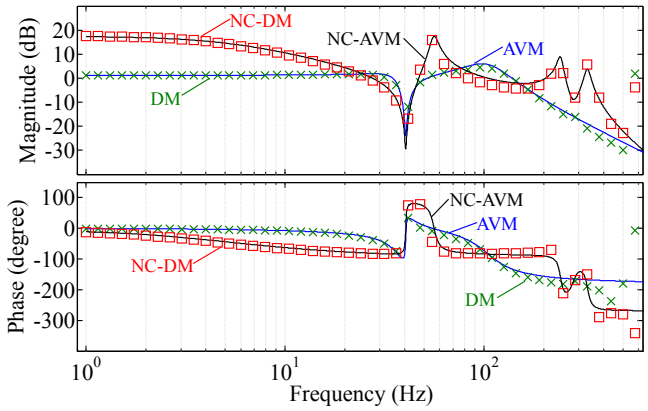

Fig. 12. Frequency response of the AVM and the DM controlled thyristor rectifier systems and non-controlled thyristor rectifier systems (NC-AVM and NC-DM).

The small-signal models derived in Section V have been used to obtain the AVM transfer function, while the PSIM frequency sweep is used to get the DM frequency response. The results of the controlled diode rectifier system are presented in Fig. 11, and Fig. 12 shows the frequency response of the controlled thyristor rectifier system. From these results it can be concluded that the AVM response fits with reasonable accuracy the DM response. However, it can be observed that the AVM response differs for frequencies close to the switching frequency (600 Hz for the 12-pulse rectifier). This is due to the assumptions considered for the development of the AVM, which are no valid for frequencies close to and above the switching frequency [18].

In order to carry out the open-loop analysis of the proposed model, the frequency response of the non-controlled AVM and DM diode rectifier systems is also shown in Fig. 11 (NC-AVM and NC-DM, respectively). These responses have been obtained using an AC grid connected to the capacitor bank bus, being the grid impedance parameters r=0.005 p.u.

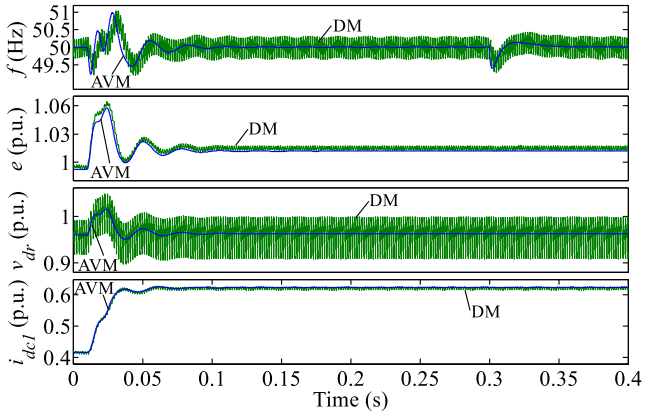

Fig. 13. Frequency, voltage magnitude at the capacitor bank bus and rectifier DC voltage and current during active- and reactive-power changes in the diode rectifier system for the AVM and DM.

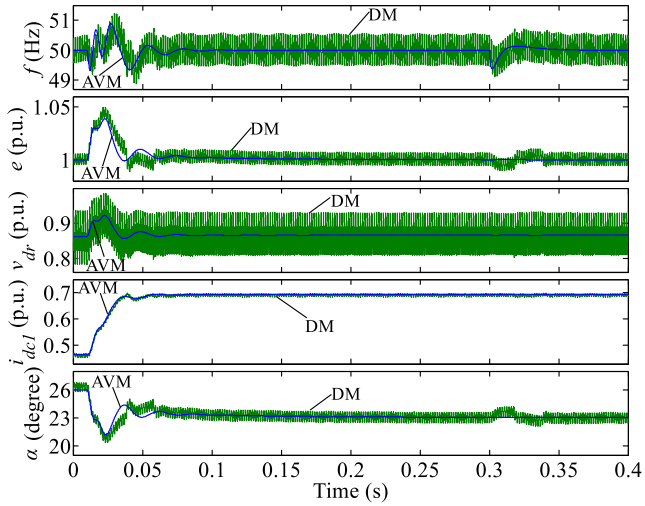

Fig. 14. Frequency, voltage magnitude at the capacitor bank bus and rectifier DC voltage, DC current and firing angle during active- and reactive-power changes in the thyristor rectifier system for the AVM and DM.

and x=0.05 p.u. The transfer function between i_{dc1} and the magnitude of the AC voltage source is analyzed. The same studies are shown in Fig. 12 for the thyristor rectifier system. Both frequency responses lead to the conclusions previously depicted for the controlled systems.

B. Large-Signal Time-Domain Analysis

The active and reactive power changes considered in Section VI are scheduled for the DM in PSIM, taking only the initial operating point of 0.4 p.u. of active power.

Fig. 13 shows the dynamic response of frequency, AC voltage magnitude, rectifier DC voltage and rectifier DC current for both the DM and the AVM in the diode rectifier system. Likewise, Fig. 14 presents the results for the thyristor rectifier system, in which firing angle α is also plotted. The DM's responses allow it to be stated that the proposed AVM represents with reasonable accuracy the response of both systems, as can be observed in Fig. 13 and Fig. 14. Moreover, the DM's responses also demonstrate that the proposed control systems show a good performance when applied to the detailed switching model, which validates the proposed control scheme.

VIII. Fault Response Study

In this section the DM of controlled diode and thyristor rectifier systems has been used to obtain the response to a fault in the capacitor bank bus at t=0.4 s during 100 ms. The pre-fault condition is set at 0.6 p.u. active power, given that the fault is scheduled after the simulations of Section VII-B.

Fig. 15 shows the diode rectifier fault response. From top to bottom frequency, AC voltage magnitude, rectifier DC voltage and rectifier DC current are depicted. During the fault AC voltage drops to zero, blocking the diode rectifier while the DC voltage oscillates at its natural frequency. Once the fault is cleared, voltage is recovered and frequency is taken to rated by the control system. The frequency signal shown in Fig. 15 is obtained by means of a PLL, because frequency is not an explicit signal in the proposed control system. This is why during the fault, with no voltage, frequency measurement is 50 Hz. Of course, the response during the fault and post-fault

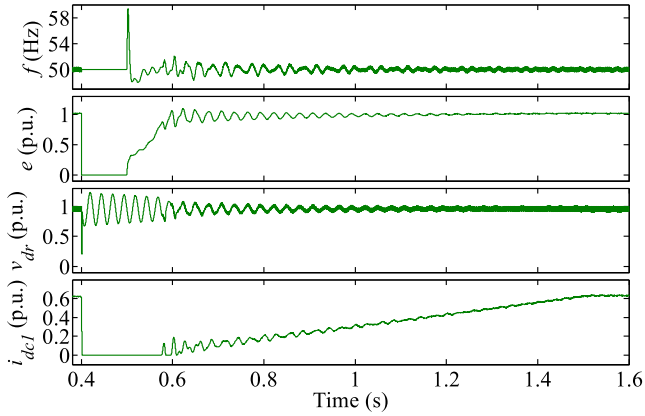

Fig. 15. Frequency, voltage magnitude at the capacitor bank bus and rectifier DC voltage and current response to a 100 ms fault in the capacitor bank bus of the DM diode rectifier system.

is very dependent on the so-called low voltage ride through response of the wind turbines. Here, the wind turbine active power is taken to zero during the fault and it is ramped up when the fault is cleared. This is the reason for the rectifier DC current increasing at a constant rate after the fault is cleared.

Fig. 16 shows the thyristor rectifier fault response. The same variables as above are shown, but also adding the rectifier firing angle. The same conclusions stated for the diode rectifier case can be established here, except that the voltage control tries to increase the firing angle during the fault in order to maintain constant voltage. However, this is not possible because of the fault and the controller reaches saturation. Once the fault is cleared, the voltage control takes over and the firing angle reaches the same value as in the pre-fault operating conditions.

IX. Conclusion

This paper has presented a novel control strategy for voltage and frequency which allows an OWF to operate connected to an LCC rectifier station in an HVDC link. This control system

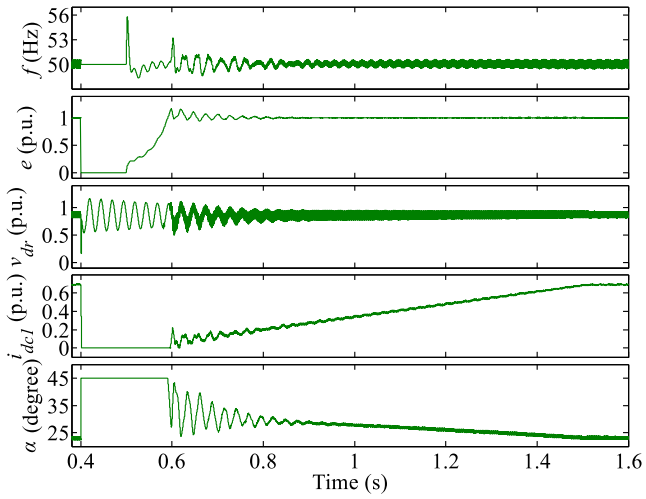

Fig. 16. Frequency, voltage magnitude at the capacitor bank bus and rectifier DC voltage, DC current and firing angle response to a 100 ms fault in the capacitor bank bus of the DM thyristor rectifier system.

has been derived from a new AVM of the LCC rectifier station. Two cases have been considered for the rectifier station: diode rectifier and thyristor rectifier. The main contribution of the proposed AVM is that active and reactive power are used as inputs and that the state variables are the polar coordinates of the capacitor-bank-bus voltage vector, i.e. voltage angle and voltage magnitude, in order to make it possible to implement a decoupled voltage and frequency control strategy in the OWF. Furthermore, the accuracy of the AVM has been verified by comparing the small-signal frequency-domain and large-signal time-domain analysis responses of the AVM and the DM. This validation also demonstrates the performance of the proposed control using a DM. Finally, a fault study has also been performed, which demonstrates that the control system is able to recover voltage and frequency within the OWF as soon as the fault is cleared. In conclusion, simulation results validate appropriate performance of the system proposed to control voltage and frequency in the AC grid of an OWF connected by an HVDC link.

APPENDIX A

The parameters of the diode rectifier station are given in Table I. These parameters are the same for the thyristor rectifier case, except that the onshore DC voltage v_{di} is 0.855 p.u. Additionally, the voltage controller parameters are k_p^e=1.67 rad/p.u. and k_i^e=0.177 rad/p.u.

APPENDIX B

The extra algebraic expressions which fully define (4) are as follows:

$$V_{dr} = \frac{3\sqrt{2}}{\pi} n_b E \cos\alpha - n_b R_\mu I_{dc1} \tag{B.1}$$

$$n_b R_\mu I_{dc1} = \frac{\frac{3\sqrt{2}}{\pi} n_b E}{2} (\cos\alpha - \cos(\alpha+\mu)) \tag{B.2}$$

TABLE I
DIODE RECTIFIER STATION PARAMETERS

Parameter	Value
n_b	2 6-pulse bridges
$S_{base,ac}$	1000 MVA
$V_{base,ac}$	211.42 kV
$P_{base,dc}$	1000 MW
$V_{base,dc}$	571.0346 kV
$\frac{x_t}{n_b}$	0.1505 p.u.
b_c	0.625 p.u.
r_{dc1}=r_{dc2}	0.00765 p.u.
l_{dc1}=l_{dc2}	0.57367 p.u.
c_c	2.66347 p.u.
f_0	50 Hz
v_{di}	0.9529 p.u.
k_p^f	1.8 p.u.
k_i^f	180/ω_0= 0.573 p.u.

$$k_{\alpha,\mu} = \frac{1}{2}(\cos\alpha + \cos(\alpha+\mu)) \cdot \sqrt{1 + (\mu\csc\mu\csc\lambda - \cot\lambda)^2} \tag{B.3}$$

where R_μ=$\frac{3}{\pi}\omega_0 L_t$ is the commutating resistance, ω_0 is the AC system frequency and λ=2α+μ.

APPENDIX C

The base magnitudes for the AC-DC per-unit system are as follows:

$$S_{base,ac} = \sqrt{3} V_{base,ac} I_{base,ac} \tag{C.1}$$

$$P_{base,dc} = S_{base,ac} = V_{base,dc} I_{base,dc} \tag{C.2}$$

$$V_{base,dc} = \frac{3\sqrt{2}}{\pi} n_b V_{base,ac} \tag{C.3}$$

$$I_{base,ac} = \frac{\sqrt{6}}{\pi} n_b I_{base,dc} \tag{C.4}$$

$$Z_{base,ac} = \frac{V_{base,ac}^2}{S_{base,ac}} \tag{C.5}$$

$$R_{base,dc} = \frac{V_{base,dc}}{I_{base,dc}} = \left(\frac{3\sqrt{2}}{\pi} n_b\right)^2 Z_{base,ac} \tag{C.6}$$

The per-unit values for the DC inductance, the DC capacitance and the commutation resistance are as follows:

$$l_{dci} = \omega_0 \frac{L_{dci}}{R_{base,dc}} = \omega_0 \frac{R_{dci}\tau_{dci}}{R_{base,dc}} = \tau_{dci}\omega_0 r_{dci}, \quad (i=1,2) \tag{C.7}$$

$$r_\mu = \frac{n_b R_\mu}{R_{base,dc}} = \frac{n_b \frac{3}{\pi}\omega_0 L_t}{\left(\frac{3\sqrt{2}}{\pi} n_b\right)^2 \omega_0 L_{base}} = \frac{\pi}{6}\frac{x_t}{n_b} \tag{C.8}$$

$$c_c = \omega_0 C_c R_{base,dc} \tag{C.9}$$

The algebraic expressions needed for the system are as follows:

$$r_\mu i_{dc1} = \frac{e}{2}(\cos\alpha - \cos(\alpha+\mu)) \tag{C.10}$$

$$v_{dr} = k_{\alpha,\mu} e \cos\varphi = e\cos\alpha - r_\mu i_{dc1} \tag{C.11}$$

$$i_r = k_{\alpha,\mu} i_{dc1} \tag{C.12}$$

REFERENCES

[1] R. Perveen, N. Kishor, and S. R. Mohanty, "Off-shore wind farm development: Present status and challenges," *Renewable and Sustainable Energy Reviews*, vol. 29, pp. 780–792, 2014.

[2] M. Bahrman and B. Johnson, "The abcs of hvdc transmission technologies," *IEEE power and energy magazine*, vol. 2, no. 5, pp. 32–44, 2007.

[3] P. Menke, R. Zurowski, T. Christ, S. Seman, G. Giering, T. Hammer *et al.*, "Breakthrough in dc grid access technology for large scale offshore wind farms," *EWEA offshore, Copenhagen, Denmark*, 2015.

[4] C. Prignitz, H.-G. Eckel, and H.-J. Knaak, "Dfig wind turbines operating in a fixed reference frame," in *Power Electronics and Applications (EPE'15 ECCE-Europe), 2015 17th European Conference on*. IEEE, 2015, pp. 1–8.

[5] T. H. Nguyen, D.-C. Lee, and C.-K. Kim, "A series-connected topology of a diode rectifier and a voltage-source converter for an hvdc transmission system," *Power Electronics, IEEE Transactions on*, vol. 29, no. 4, pp. 1579–1584, 2014.

[6] D. Xiang, L. Ran, J. R. Bumby, P. J. Tavner, and S. Yang, "Coordinated control of an hvdc link and doubly fed induction generators in a large offshore wind farm," *Power Delivery, IEEE Transactions on*, vol. 21, no. 1, pp. 463–471, 2006.

[7] R. Li, S. Bozhko, G. Asher, J. Clare, L. Yao, and C. Sasse, "Grid frequency control design for offshore wind farms with naturally commutated hvdc link connection," in *Industrial Electronics, 2006 IEEE International Symposium on*, vol. 2. IEEE, 2006, pp. 1595–1600.

[8] R. Li, S. Bozhko, and G. Asher, "Frequency control design for offshore wind farm grid with lcc-hvdc link connection," *Power Electronics, IEEE Transactions on*, vol. 23, no. 3, pp. 1085–1092, 2008.

[9] R. Blasco-Gimenez, S. Ano-Villalba, J. Rodriguez-D'Derlee, F. Morant, and S. Bernal-Perez, "Distributed voltage and frequency control of offshore wind farms connected with a diode-based hvdc link," *Power Electronics, IEEE Transactions on*, vol. 25, no. 12, pp. 3095–3105, 2010.

[10] R. Blasco-Gimenez, S. Ano-Villalba, J. Rodriguez-D'Derlee, S. Bernal-Perez, and F. Morant, "Diode-based hvdc link for the connection of large offshore wind farms," *Energy Conversion, IEEE Transactions on*, vol. 26, no. 2, pp. 615–626, 2011.

[11] H. Zhou, G.-M. Yang, J. Wang, and H. Geng, "Control of a hybrid high-voltage dc connection for large doubly fed induction generator-based wind farms," *Renewable Power Generation, IET*, vol. 5, no. 1, pp. 36–47, 2011.

[12] S. V. Bozhko, R. Blasco-Gimenez, R. Li, J. C. Clare, and G. M. Asher, "Control of offshore dfig-based wind farm grid with line-commutated hvdc connection," *Energy Conversion, IEEE Transactions on*, vol. 22, no. 1, pp. 71–78, 2007.

[13] R. E. Torres-Olguin, A. Garces, M. Molinas, and T. Undeland, "Integration of offshore wind farm using a hybrid hvdc transmission composed by the pwm current-source converter and line-commutated converter," *Energy Conversion, IEEE Transactions on*, vol. 28, no. 1, pp. 125–134, 2013.

[14] S. Chiniforoosh, J. Jatskevich, A. Yazdani, V. Sood, V. Dinavahi, J. Martinez, and A. Ramirez, "Definitions and applications of dynamic average models for analysis of power systems," *IEEE Transactions on Power Delivery*, vol. 25, no. 4, pp. 2655–2669, 2010.

[15] S. D. Sudhoff and O. Wasynczuk, "Analysis and average-value modeling of line-commutated converter-synchronous machine systems," *IEEE transactions on energy conversion*, vol. 8, no. 1, pp. 92–99, 1993.

[16] S. Sudhoff, K. A. Corzine, H. Hegner, and D. Delisle, "Transient and dynamic average-value modeling of synchronous machine fed load-commutated converters," *IEEE Transactions on Energy Conversion*, vol. 11, no. 3, pp. 508–514, 1996.

[17] J. Alt, S. Sudhoff, and B. Ladd, "Analysis and average-value modeling of an inductorless synchronous machine load commutated converter system," *IEEE transactions on energy conversion*, vol. 14, no. 1, pp. 37–43, 1999.

[18] J. Jatskevich, S. D. Pekarek, and A. Davoudi, "Parametric average-value model of synchronous machine-rectifier systems," *IEEE transactions on energy conversion*, vol. 21, no. 1, pp. 9–18, 2006.

[19] ——, "Fast procedure for constructing an accurate dynamic average-value model of synchronous machine-rectifier systems," *IEEE Transactions on Energy Conversion*, vol. 21, no. 2, pp. 435–441, 2006.

[20] H. Atighechi, S. Chiniforoosh, J. Jatskevich, A. Davoudi, J. Martinez, M. Faruque, V. Sood, M. Saeedifard, J. Cano, J. Mahseredjian *et al.*, "Dynamic average-value modeling of cigre hvdc benchmark system," *IEEE Transactions on Power Delivery*, vol. 29, no. 5, pp. 2046–2054, 2014.

[21] H. Atighechi, F. Therrienl, S. A. Akbarabadi, S. Chiniforoosh, and J. Jatskevich, "Using current-source formulation for dynamic average-value modeling of inverter side hvdc system," in *Electrical and Computer Engineering (CCECE), 2013 26th Annual IEEE Canadian Conference on*. IEEE, 2013, pp. 1–4.

[22] H. Atighechi, S. Chiniforoosh, S. Ebrahimi, and J. Jatskevich, "Using multiple reference frame theory for considering harmonics in average-value modeling of diode rectifiers," *IEEE Transactions on Energy Conversion*, vol. 31, no. 3, pp. 872–881, 2016.

[23] S. Chiniforoosh, H. Atighechi, A. Davoudi, J. Jatskevich, A. Yazdani, S. Filizadeh, M. Saeedifard, J. Martinez, V. Sood, K. Strunz *et al.*, "Dynamic average modeling of front-end diode rectifier loads considering discontinuous conduction mode and unbalanced operation," *IEEE Transactions on Power Delivery*, vol. 27, no. 1, pp. 421–429, 2012.

[24] K. Chaijarurnudomrung, K.-N. Areerak, and K.-L. Areerak, "Modeling of three-phase controlled rectifier using a dq method," in *Advances in Energy Engineering (ICAEE), 2010 International Conference on*. IEEE, 2010, pp. 56–59.

[25] E. W. Kimbark, *Direct current transmission*. John Wiley & Sons, 1971, vol. 1.

[26] M. Daryabak, S. Filizadeh, J. Jatskevich, A. Davoudi, M. Saeedifard, V. Sood, J. Martinez, D. Aliprantis, J. Cano, and A. Mehrizi-Sani, "Modeling of lcc-hvdc systems using dynamic phasors," *IEEE Transactions on Power Delivery*, vol. 29, no. 4, pp. 1989–1998, 2014.

[27] Y. Huang, S. Ebrahimi, N. Amiri, H. Atighechi, and J. Jatskevich, "A parametric dynamic phasor model of line-commutated rectifier systems," in *Electrical and Computer Engineering (CCECE), 2016 IEEE Canadian Conference on*. IEEE, 2016, pp. 1–4.

[28] Y. Huang, M. Chapariha, S. Ebrahimi, N. Amiri, and J. Jatskevich, "Interfacing sfa-and gam-type dynamic phasors for modeling of integrated ac-dc power systems," in *Power and Energy Society General Meeting (PESGM), 2016*. IEEE, 2016, pp. 1–5.

[29] L. M. Castro, E. Acha, and C. R. Fuerte-Esquivel, "A novel vsc-hvdc link model for dynamic power system simulations," *Electric Power Systems Research*, vol. 126, pp. 111–120, 2015.

[30] M. Guan, W. Pan, J. Zhang, Q. Hao, J. Cheng, and X. Zheng, "Synchronous generator emulation control strategy for voltage source converter (vsc) stations," *IEEE Transactions on Power Systems*, vol. 30, no. 6, pp. 3093–3101, 2015.

[31] M. Szechtman, T. Wess, and C. Thio, "A benchmark model for hvdc system studies," in *AC and DC Power Transmission, 1991., International Conference on*. IET, 1991, pp. 374–378.

[32] X.-F. Wang, Y. Song, and M. Irving, *Modern power systems analysis*. Springer Science & Business Media, 2010.

[33] J. L. Rodriguez-Amenedo, S. Arnalte, and J. C. Burgos, "Automatic generation control of a wind farm with variable speed wind turbines," *Energy Conversion, IEEE Transactions on*, vol. 17, no. 2, pp. 279–284, 2002.

[34] E.-E. ENTSO-E, "Network code for requirements for grid connection applicable to all generators (nc rfg), march 2013.[online]. available: h ttp," *networkcodes. entsoe. eu/connectioncodes*.

[35] R. Blasco-Gimenez, N. Aparicio, S. Ano-Villalba, and S. Bernal-Perez, "Lcc-hvdc connection of offshore wind farms with reduced filter banks," *IEEE Transactions on Industrial Electronics*, vol. 60, no. 6, pp. 2372–2380, 2013.